Energy Conversion and Management 247 (2021) 114754

Contents lists available at ScienceDirect

Energy Conversion and Management

journal homepage: www.elsevier.com/locate/enconman

Segmental material design in thermoelectric devices to boost heat-to-electricity performance

Junwei Zhao [a], Wei Xu [a], Zhengfei Kuang [b], Rui Long [a,*], Zhichun Liu [a], Wei Liu [a]

[a] School of Energy and Power Engineering, Huazhong University of Science and Technology, Wuhan 430074, China
[b] Wuhan Second Ship Design and Research Institute, Wuhan 430074, China

ARTICLE INFO

Keywords:
Segmented thermoelectric generator
Machine learning
Energy conversion efficiency
Electric power

ABSTRACT

In this study, a seven-layer segmented thermoelectric generator (STEG) is presented with four pairs of TE materials imposed on each semiconductor leg. Firstly, the performance of the STEG with every possible combination (16384 material sequences) of the leg materials for either leg is analyzed when the other leg is equipped with selected material. Machine learning is further employed to reveal the relationship of the electric power and the energy conversion efficiency with the leg material sequences via the ensemble-based regression model whose hyper-parameters are adjusted by the Bayesian optimization. The criteria of maximum output power and maximum energy conversion efficiency are employed to identify the optimal material sequences for each semiconductor leg, thus the overall optimal material sequences. Comparing to the traditional TEG, when operating between 600 K and 293 K, the electric power and energy conversion efficiency of STEG is 184.1 mW and 16.7%, which presents enhancement of 86.14% and 31.19%, respectively. Counterintuitively, the optimal sequence does not arrange in strict conformity with *ZT* value which has never been reported in the previous studies. The underling mechanisms are revealed via analyzing the temperature distribution, electric resistance, *ZT* value and voltage of each layers. The results in this study contributes to the rational design and fabrication of satisfied STEGs.

1. Introduction

Since the second industrial revolution, the demand for energy has been increasing for over 150 years and the trend is continuing. Fossil fuel is the main source of energy for human beings. However, fossil fuels are non-renewable whose exploitation and utilization are destructive to the natural environment. The exploitation of green and clean energy is highly demanded [1–5]. More than 90% of the energy used by human beings is related to thermal process, most of which is rejected in the form of low-grade waste heat during the utilization process. Further recovery and utilizing such low-grade heat energy act as an important supplement to energy demand [6,7]. Thermoelectric generator (TEGs) is the simplest and direct way to those waste heat. Through the Seebeck effect, electric voltage is established induced by the temperature difference imposed on the semiconductor ends. TEG has no moving parts and features quick response, all solid state, it has been applied in many fields, such as military, aerospace, agriculture, daily life, and medical etc [8–14].

The figure of merit *ZT* is applied to evaluate the performance of TE material, $ZT = \alpha^2\sigma T/\lambda$, where α is the Seebeck coefficient, σ is the electric conductivity, λ is the thermal conductivity, and *T* is the absolute temperature of the material. Generally, thermoelectric material with large *ZT* means high output power and energy conversion efficiency. In the last few decades, a tremendous amount of work has gone into enhancing the *ZT* of TE materials, and there are two directions of their work. On the one hand, fabricating TE materials by doping simple substance or compounds into common *TE* material and finding new TE material, TE materials with higher *ZT* value have better performance in output power and electric conductivity theoretically. But *ZT* value depends on Seebeck coefficient, electric conductivity and thermal conductivity, but generally these variables are contradictory. Various TE materials were studied and applied to enhance the performance of TEG including Bi_2Te_3 [15–19], PbTe[20,21], $Ca_xCo_4Sb_{12}$ [22], and $Ca_5Al_2Sb_6$ [23].

On the other hand, changing the structures of semiconductor legs including cylindrical legs, cone-shaped legs and asymmetrical legs, segmented thermoelectric generators (STEG) offer alternative ways to improve the performance of TEG [24–27]. As the evaluation index of the performance of TE material, *ZT* value varies with the temperature, but the *ZT* value of each material is high within a narrow temperature, when

* Corresponding author.
E-mail address: r_long@hust.edu.cn (R. Long).

https://doi.org/10.1016/j.enconman.2021.114754
Received 31 March 2021; Accepted 10 September 2021
Available online 21 September 2021
0196-8904/© 2021 Elsevier Ltd. All rights reserved.

Nomenclature

A	Material A
B	Material B
C	Material C
D	Material D
J	current density vector (Am^{-2})
N_i	Layer i of N-type
R	electrical resistance (Ω)
P	Power output(W)
P_i	Layer i of P-type
P_{max}	maximum output power(W)
T	Temperature(K)
T_H	Temperature of hot side(K)
Tc	Temperature of cold side(K)
ZT	thermoelectric figure of merit

Greek letters

α	Seebeck coefficient (VK^{-1})
σ	electric conductivity (Sm^{-1})
λ	thermal conductivity (Wm^{-1} K^{-1})
β	average Thomson coefficient (VK^{-2})
η	Efficiency (%)
Φ	Electrical scalar potential(V)

Subscripts

i	Layer i
H	Hot side
C	Cold side
max	maximum

Abbreviation

STEG	segmented thermoelectric generator
TEG	thermoelectric generator
TEC	thermoelectric cooler
Opt	optimized

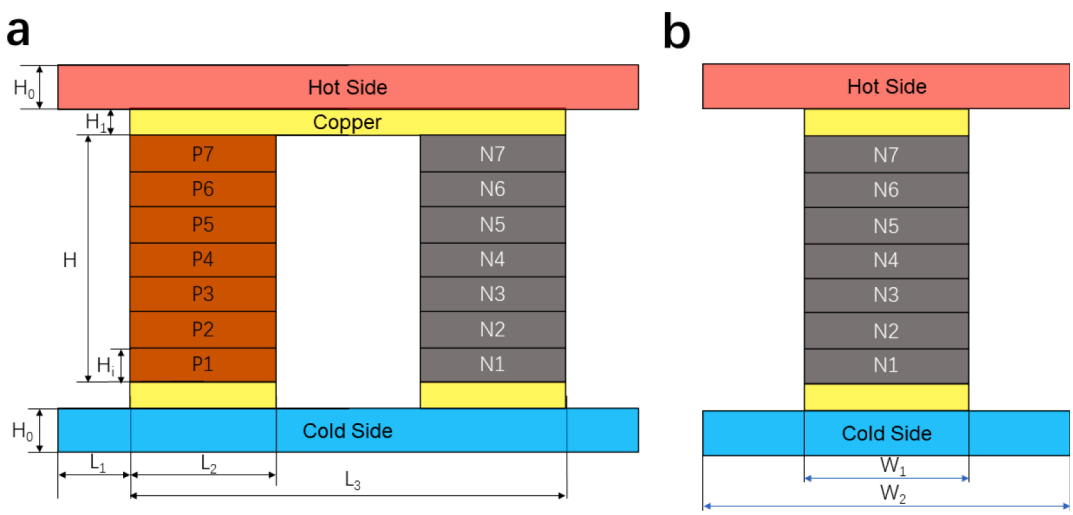

Fig. 1. The front view of the seven-layer STEG(a) and the side view of the seven-layer STEG(b).

Table 1
Dimensions of the seven-layer STEG.

H_0	0.3 mm
H_1	0.1 mm
H_i	1.7/7mm
H	1.7 mm
L_1	0.75 mm
L_2	1 mm
L_3	2.5 mm
W_1	1.2 mm
W_2	3 mm

the temperature is out of the proper range of a kind of TE material, there will be a remarkable decrease of its *ZT* value. Generally, temperature difference between hot side and cold side of TEG exceed 200 K, which also exceed the favorable temperature range of most TE materials. Thus, STEG is designed for high energy conversion efficiency for a wide range of operating temperatures., Lei Zhu et al. [28] reported that a both-segmented TEG had maximum energy conversion efficiency of 9.15% for a temperature difference of 350 K which is 16% higher than traditional TEG. Li et al. [29] fabricated a STEG which had a maximum output power of 48.6 mV at a temperature difference of 296 K, the voltage of STEG was 17.4% less than theoretical value, which demonstrate that STEG is feasible and promising way to improve performance of TEG. Shen et al. [30] proposed a segmented annular thermoelectric generator and studied the influences of annular shape parameter, height ratios of high temperature segment to leg in P-type and N-type legs, temperature ratio on the performance of their device, results show that the superiority of their device becomes visible with the rising temperature ratio. Liu et al. [31] proposed a novel solar thermoelectric generator design which combines segmented thermoelectric materials and asymmetrical legs with variable cross-sectional area along the leg length, their results shows that the segmented design increases the output power by 14.9% and 16.6%. Lundgaard et al. [32] optimized the cooling power and efficiency (coefficient of performance) of thermoelectric coolers by spatially distributing two different thermoelectric materials in a two-dimensional design space, demonstrated that the cooling power and efficiency can be improved by 48.7% and 11.4%.

The output electric power and energy conversion efficiency can be enhanced by segmented designs. In previous studies regarding the STEG, the number of layer of the semiconductor legs is less than 5 and the leg materials are limited [28,33,34]. The material of each layer is the same,

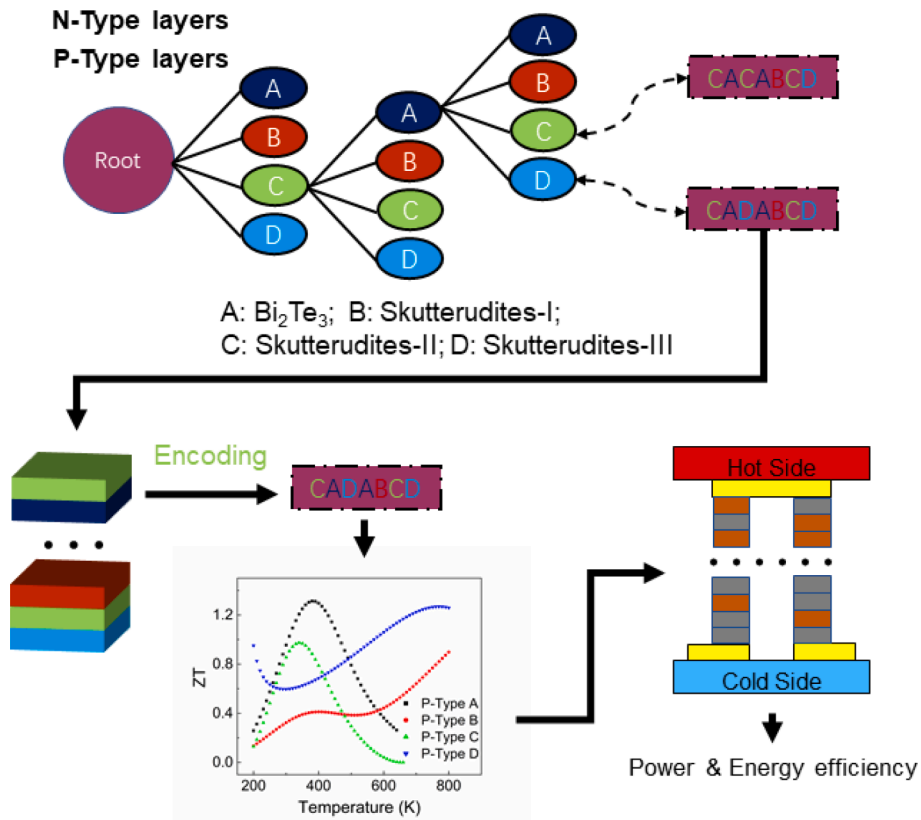

Fig. 2. Schematic of the calculation process.

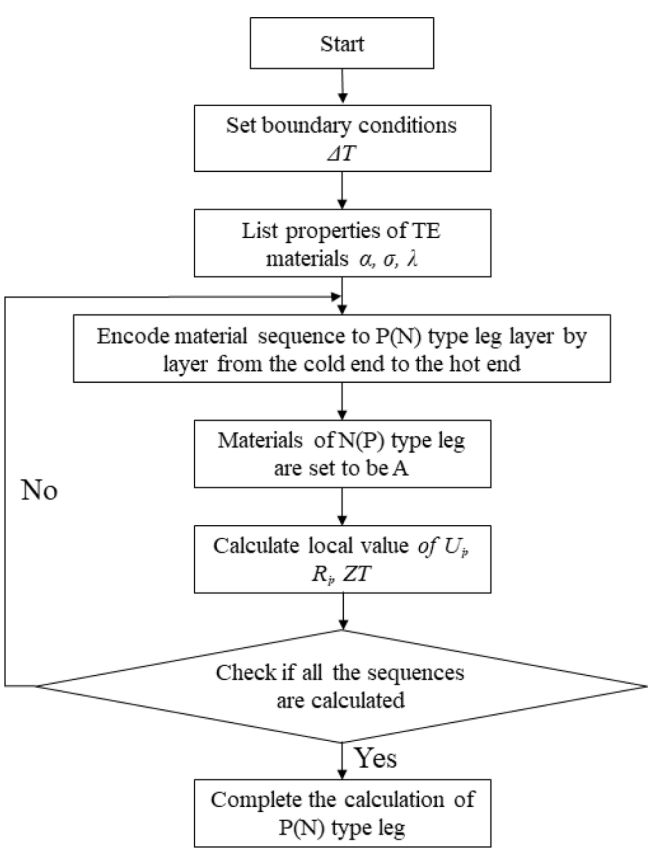

Fig. 3. Calculation flowchart.

such as n-type Bi_2Te_3 in the n-leg layer and p-type Bi_2Te_3 in the p-leg layer. The asymmetric distribution has not been considered. In present study, in consideration of the calculation resources, a seven-layer STEG is presented with four pairs of TE materials imposed on semiconductor legs. Firstly, the performance of the STEG with every possible combination (16384 material sequences) of the leg materials for either leg is analyzed when the other leg is equipped with selected material. Machine learning is further employed to reveal the relationship of the electric power and the energy conversion efficiency with the leg material sequences via the ensemble-based regression model. The criteria of maximum output power and maximum energy conversion efficiency are employed to identify the optimal material sequences for each semiconductor leg, thus the overall optimal material sequences. The temperature distribution, electric resistance, *ZT* value and voltage of each layer and the entire leg under the original, and partly optimized and overall optimized configures are systematically investigated. Counter-intuitive phenomenon is encountered and the underling mechanisms are revealed.

2. System description

Generally, a TEG device is constructed by tens or hundreds of units that consists of two electric insulating ceramic plates, three metallic connectors(copper), a P-type and an N-type semiconductor legs. As is shown in Fig. 1, each leg is of Length = 1 mm, Width = 1.2 mm, and Height = 1.7 mm, and the conductor of the legs is copper. Dimensions of the seven-layer STEG is shown in Table 1

During the simulation, the temperature of hot surface and cold surface is constant, in addition, the adiabatic walls are regarded as lateral surfaces. The entire calculation process is shown in Fig. 2. There are four pairs of TE materials in this study, including A(P-type and N-type Bi_2Te_3), B(P-type and N-type Skutterudites), C(a commercial bismuth telluride TEM from Fuxin Co. China) [35], and D(P-type $DD_{0.59}Fe_{2.7}Co_{1.3}Sb_{11.8}Sn_{0.2}$ and N-type :$(Sr,Ba,Yb)_yCo_4Sb_{12}$ + 9.1%$In_{0.4}Co4Sb_{12}$)

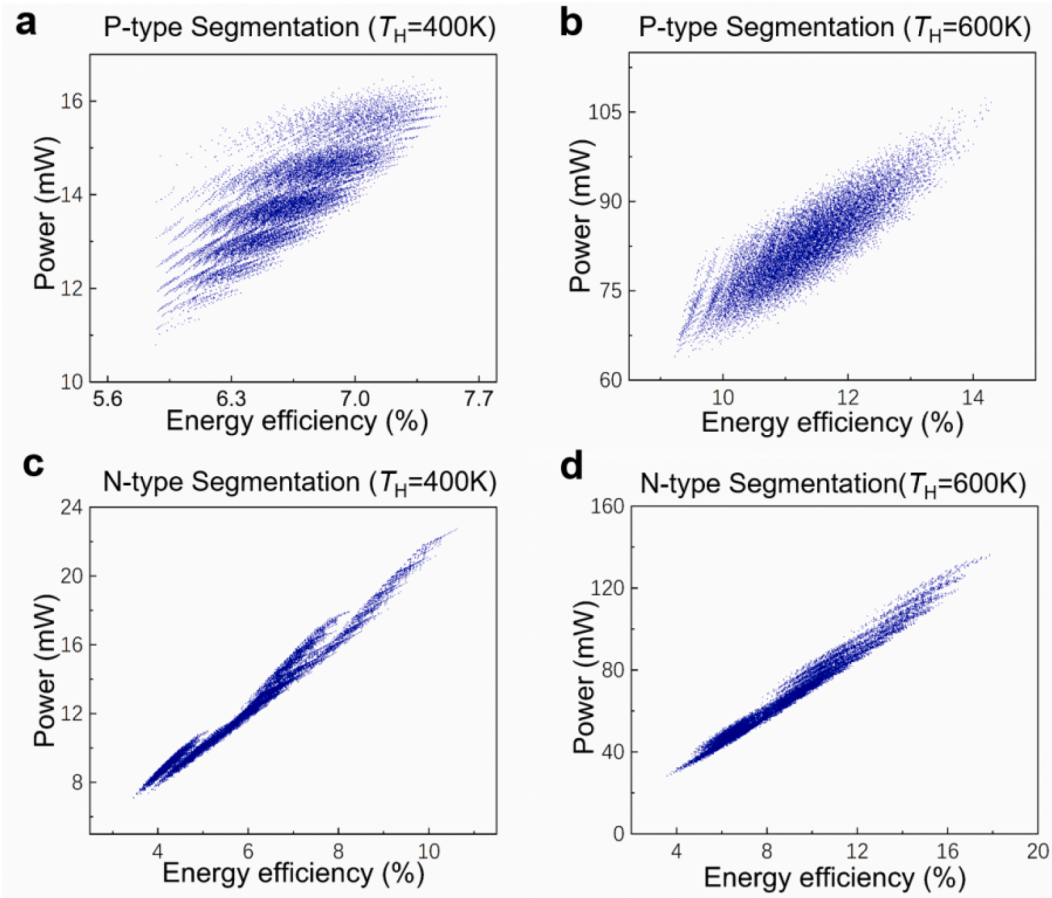

Fig. 4. (a) Power and energy efficiency of all P-type sequences when $T_H = 400$ K; (b) Power and energy efficiency of all P-type sequences when $T_H = 600$ K; (c) Power and energy efficiency of all N-type sequences when $T_H = 400$ K; (d) Power and energy efficiency of all N-type sequences when $T_H = 600$ K.

Table 2
Accuracy of the machine learning results.

Machine learning objectives	RSME	R^2	MSE	MAE
Energy efficiency @T_H = 400 K	0.00021956	0.99	4.8205×10^{-8}	0.00015643
Power @T_H = 400 K	0.0010254	0.99	1.0515×10^{-6}	0.00073344
Energy efficiency @T_H = 600 K	0.0011849	1	1.4039×10^{-6}	0.00088017
Power @T_H = 600 K	0.0003903	1	1.5234×10^{-7}	0.00027581

[36], and the physical parameters of these materials are presented in Table A1–A3, then these parameters are programed in MATLAB. The calculation procedure is shown in Fig. 3. In the calculation, the temperature of hot side is set to be 400 K or 600 K. The temperature of cold side is set to be 293 K. Each semiconductor leg of the STEG is equally divided into seven layers. The material in each layer in the P-type or N-type leg is randomly selected. The material sequence is encoded layer by layer from the cold end to the hot end such as *CACABCD,* and the physical parameters of each layer are set to be variable in COMSOL. Each material sequence is coded in the MATLAB software, then the physical parameters of the for pair of TE materials are assigned to each layer in COMSOL according to the sequence and the electric power and energy conversion efficiency under each material sequence is calculated in the COMSOL software with MATLAB interface.

Heat conduction, Seebeck, Thomson, and Peltier effects, Joule heat are taken into consideration in this model. The STEG ends are heated or cooled at constant temperatures at T_H and T_C respectively. The external surface of semiconductor elements is assumed as perfectly thermal and electric insulated. And the electrical resistivity, thermal conductivity and the Seebeck and Thomson coefficients of the segment materials are homogenous and determined by temperature. Therefore, the energy governing equation are obtained as:

$$\nabla\cdot(\lambda_n\nabla T)+\frac{J^2}{\sigma_n}-\beta_n\vec{j}\cdot\nabla T=0 \tag{1}$$

$$\nabla\cdot(\lambda_p\nabla T)+\frac{J^2}{\sigma_p}-\beta_p\vec{j}\cdot\nabla T=0 \tag{2}$$

where λ is the average thermal conductivity, σ is the electrical conductivity, β is the average Thomson coefficient, J is the local current density , the subscript p and n represent P-type and N-type semiconductor legs. In Eq. (1) and Eq. (2), the first ,second and third term represent Fourier heat conduction, Joule heating and Thomson effect. $\beta = \frac{Td\alpha}{dT}$ [37]. Where α is the Seebeck coefficient, It is obvious that the Thomson coefficient is 0 when the Seebeck coefficient is temperature-independent. Although Thomson effect is the secondary effect of Seebeck effect, the ignorance of Thomson effect leads an underestimation of TEC cooling capacity [38]. Thus, in this work, the temperature-depended Seebeck coefficient and Thomson effect are taken into consideration.

The governing equation of the electric voltage can be expressed as:

$$\nabla\cdot(\sigma(\nabla\phi-\alpha\nabla T))=0 \tag{3}$$

The current density vector can be calculated by the following equation:

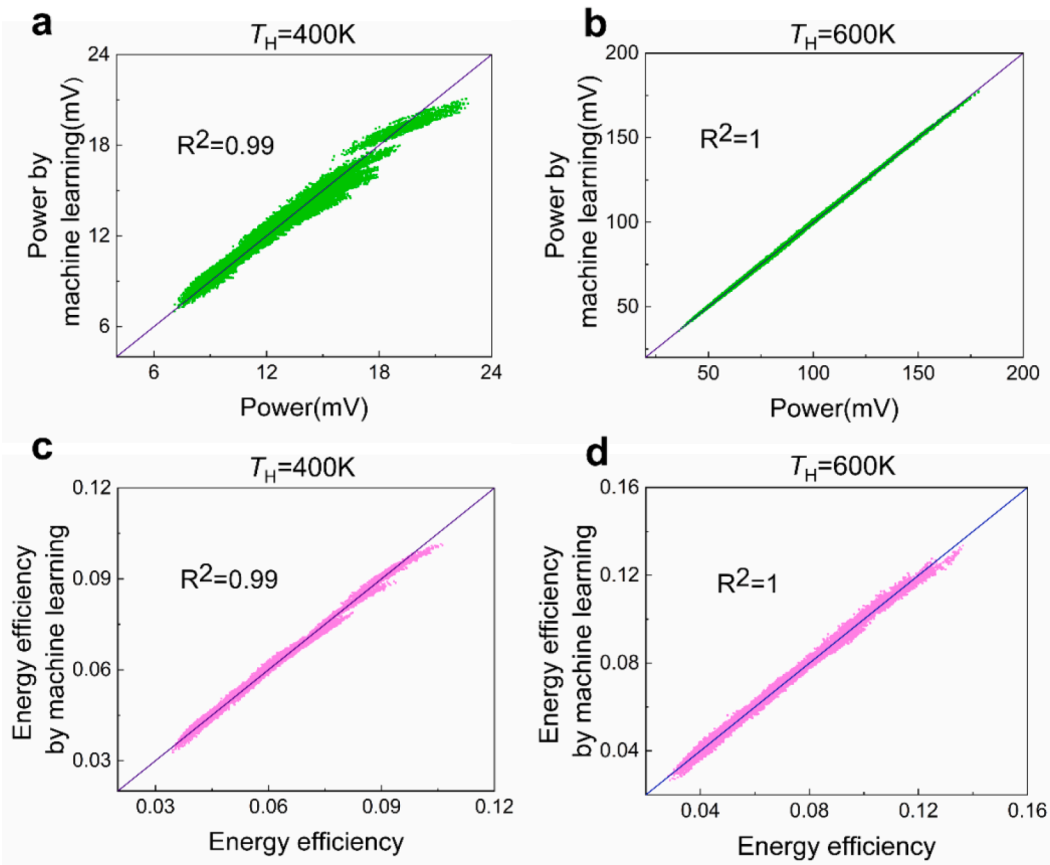

Fig. 5. (a, b) Comparison between predicted and calculated power when $T_H = 400$ K and 600 K; (c, d) Comparison between predicted and calculated energy efficiency when $T_H = 400$ K and 600 K.

Table 3
optimal material sequence under the condition of maximum electric power.

	$T_H = 400$ K	$T_H = 600$ K
P-type	*ACDAAAA*	*CCDADDD*
N-type	*AAAAAAA*	*CCDDDDD*

$$\vec{J} = \sigma\vec{E} = \sigma(-\nabla\phi + \alpha\nabla T) \tag{4}$$

The internal resistance can be obtained by the following formula:

$$R = \sum_{i=1}^{7} R_{Pi} + \sum_{i=1}^{7} R_{Ni} = \sum_{i=1}^{7}\left(\sigma_{Pi}\frac{A}{H}\right)^{-1} + \sum_{i=1}^{7}\left(\sigma_{Ni}\frac{A}{H}\right)^{-1} \tag{5}$$

The maximum output power can be obtained by open circuit voltage and internal electrical resistance. Thus, P_{max} is calculated by

$$p_{max} = \frac{U^2}{4R} \tag{6}$$

where U is the open circuit voltage.

The energy conversion efficiency under P_{max} can be expressed as:

$$\eta = \frac{P_{max}}{Q_{in}} \tag{7}$$

where Q_{in} is the heat input.

3. Results and discussion

3.1. 1 Machine learning

Each leg is equally divided into seven layers in the vertical direction. There are four pairs of TE materials in this study. According to their performance of *ZT* value at different temperature, material A and C are classified into low-temperature materials (300–500 K), B and D are usual for medium-temperature (500–900 K). The temperature depended parameters for those materials are listed in the Appendix.

The electric power and energy efficiency of the STEG with every possible combination (16384 material sequences) of the leg materials for either leg is analyzed when the other leg is equipped with selected material at different operation conditions are shown in Fig. 4. Although the material sequences with high power tend to have high efficiency, the optimal sequences leading maximum power or maximum efficiency are different (Fig. 4a and b).

Furthermore, to verify the performance of all the sequences, machine learning is employed to reveal the relationship of the electric power and the energy conversion efficiency with the leg material sequences via the ensemble-based regression model whose hyper-parameters are adjusted by the Bayesian optimization. Each machine learning process are trained several times to alleviate the random error to guarantee convincing results. Root mean square error (RMSE), R^2, MAE (mean absolute error), MSE (mean square error) are employed to describe the model accuracy (Table 2). As shown in Fig. 5, ensemble model can predict the power and energy efficiency accurately. At $T_H = 400$ K, $R^2 = 0.99$ for the power and energy efficiency predications. At $T_H = 600$ K, $R^2 = 1$ for the power and energy efficiency predications.

3.2. Performance under the maximum electric power

As shown in Table 3, under the condition of maximum electric power, the optimal material sequence of the P-type and N-type semiconductor legs are *ACDAAAA* and *AAAAAAA* when $T_H = 400$ K, the

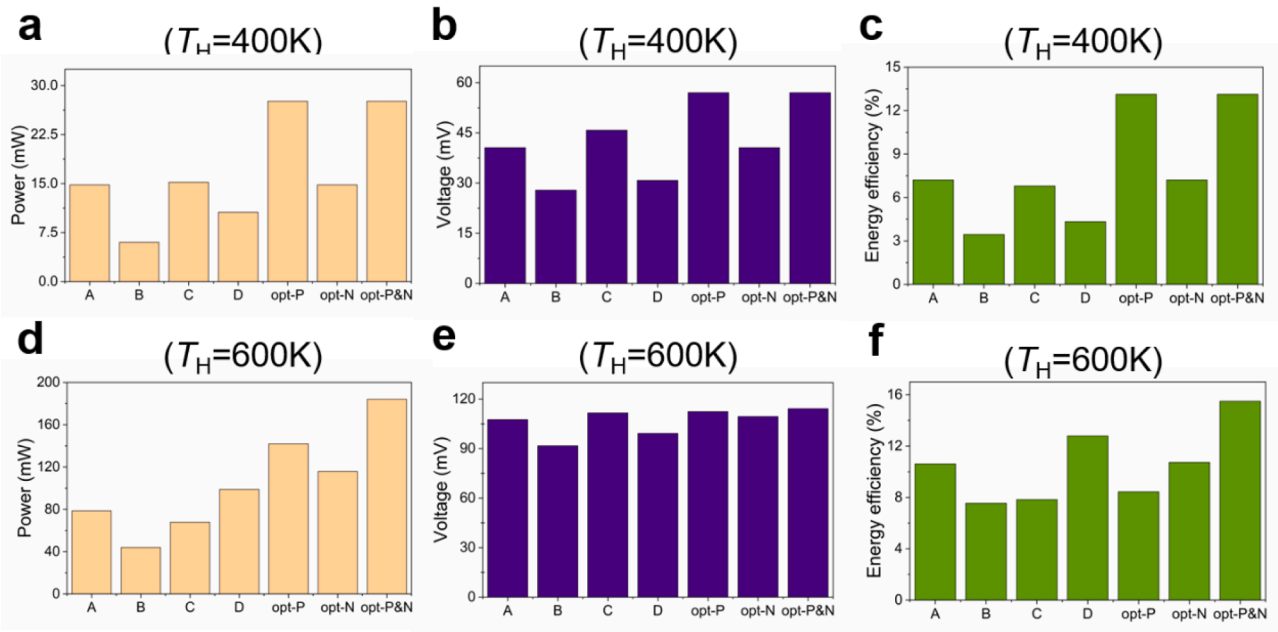

Fig. 6. Power(a, d) open circuit voltage(b, e), and energy efficiency(c, f) of different scenarios at two fixed temperature(400 K and 600 K) under the maximum power condition.

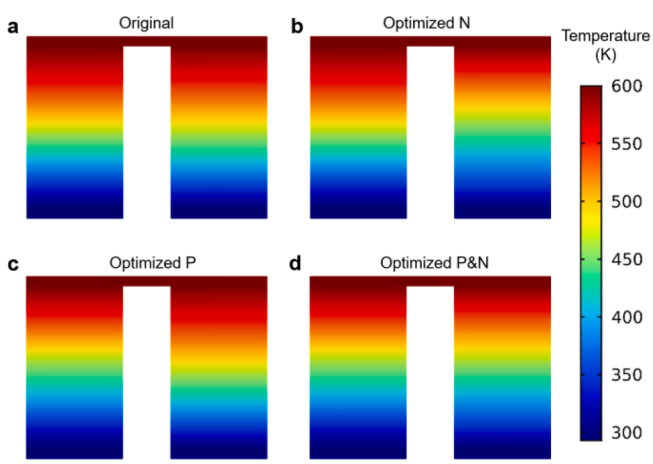

Fig. 7. Distribution of temperature of different scenarios when $T_H = 600$ K under the maximum power.

optimal material sequence of the P-type and N-type semiconductor legs are *CCDADDD* and *CCDDDDD* when $T_H = 600$ K. For comparison, the performance under A, B, C, and D materials on the entire P-type and N -type semiconductor leg are also calculated, respectively. Opt-N means that N-type semiconductor leg is set to the best sequence while P-type semiconductor layers are set to material A. Opt-P means that P-type semiconductor leg is set to the best sequence while N-type semiconductor layers are set to material A. As is shown in Fig. 6, for electric power, open circuit voltage and energy efficiency, opt-P&N is the highest and is apparently higher than B due to the fact that *ZT* value of material B is the lowest under the temperature of 273.15 K ~ 600 K. The performance of opt-P&N is totally the same as the performance of opt-P when $T_H = 400$ K due to the best sequence of N-type semiconductor legs is exactly AAAAAAA, which result in that the sequences of opt-P&N and opt-P are the same. When $T_H = 400$ K, the power of opt-P&N is 27.7 mW which is 82.24% higher than C which is highest among A, B, C and D as shown in Fig. 6a. The output open circuit voltage of opt-P&N is 57 mV which is 24.45% higher than C. The energy efficiency of opt-P&N is 13.12% which is 82.22% higher than A as shown in Fig. 6c. When $T_H = 600$ K, the power of opt-P&N is 184.1 mW which is 86.14% higher than D which is highest among A, B, C and D. The output open circuit voltage of opt-P&N is 114.2 mV which is 1.02% higher than C as shown in Fig. 6e. The energy efficiency of opt-P&N is 15.49% which is 21.11% higher than D (Fig. 6f).

Fig. 7 illustrates the inner temperature distribution of the TEG when $T_H = 600$ K. "Original" means that all semiconductor layers are set to material A. The low temperature zone has wider distribution after optimization due to the highest *ZT* value of all material mentioned in this work is under 300 ~ 450 K. After P-Type semiconductor layers are optimized, the temperature distribution of N-Type semiconductor leg is almost unchanged and there is a similar statement for P-Type semiconductor leg.

The comparisons of the electric resistance of each layer is shown in Fig. 8, we can get a similar conclusion with what is shown in Fig. 7 that after a type semiconductor layers are optimized, the electric resistance distribution of another type semiconductor leg is almost unchanged, and when $T_H = 400$ K, the N-type electric resistance of opt-P&N is 19.69 mΩ which is equal to origin, and the P-type electric resistance of opt-P&N is 9.81 mΩ which is 20.64% higher than origin. When $T_H = 600$ K, the N-type electric resistance of opt-P&N is 14.32 mΩ which is 62.97% lower than origin, and the P-type electric resistance of opt-P&N is 14.32 mΩ which is 4.24% higher than origin. It is obvious that the when T_H is at a low level, the optimization has nearly no benefit to the decrease of electric resistance, but with the raise of T_H, the total electric resistance is raising and the optimization tend to reduce the electric resistance.

Fig. 9 shows the open circuit voltage of each layer and the entire leg. The open circuit voltage of a leg remains unchanged with the optimization of another leg. When $T_H = 400$ K, the N-type open circuit voltage of opt-P&N is 22.638 mV which is equal to origin, and the P-type open circuit voltage of opt-P&N is 33.41 mV which is 99.82% higher than the origin. When $T_H = 600$ K, the N-type open circuit voltage of opt-P&N is 59.27 mV which is 3.25% higher than origin, and the P-type open circuit voltage of opt-P&N is 55 mV which is 9.17% higher than origin. Strong evidence of the increase of open circuit voltage was found after the sequence of the semiconductor legs being optimized.

To reveal the mechanism of the optimized results, Fig. 10 shows the variation in *ZT* value of each layer and the entire leg. When $T_H = 400$ K, the N-type *ZT* value of opt-P&N is 0.8383 while the origin is 0.8382, and

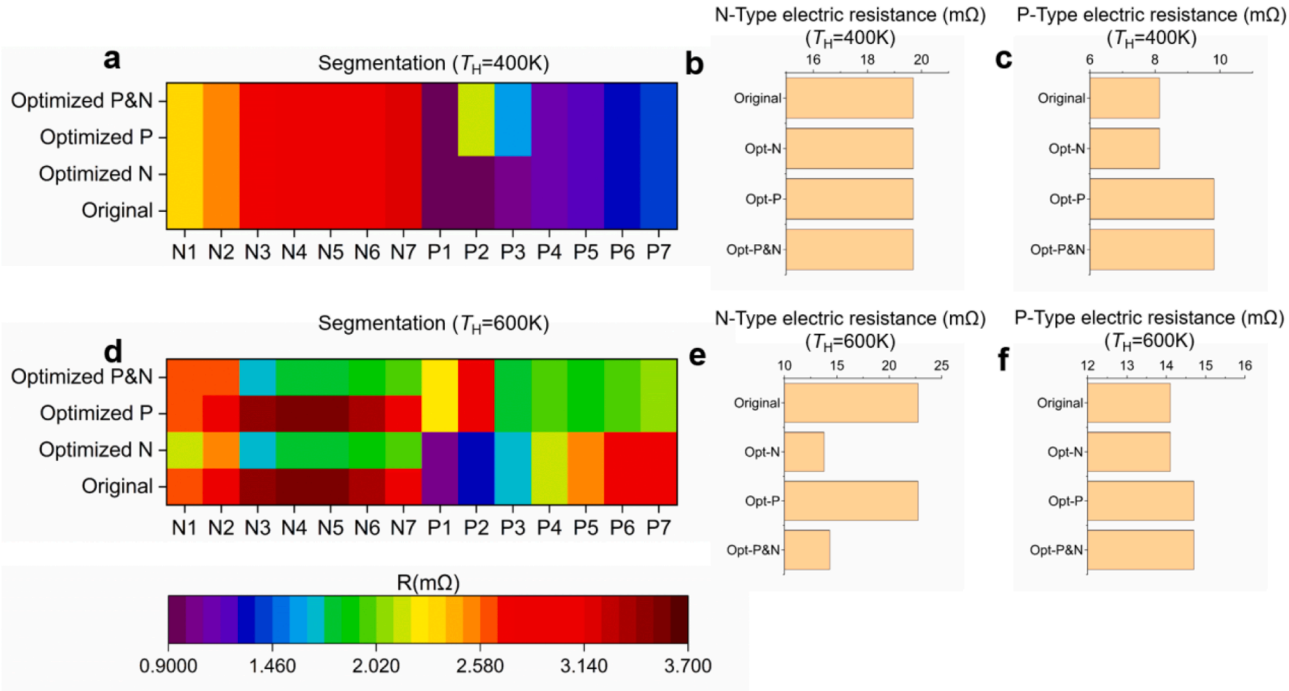

Fig. 8. Comparisons of the electric resistance of each layer (a, d) and the entire leg (b, c, e, f) under the maximum power.

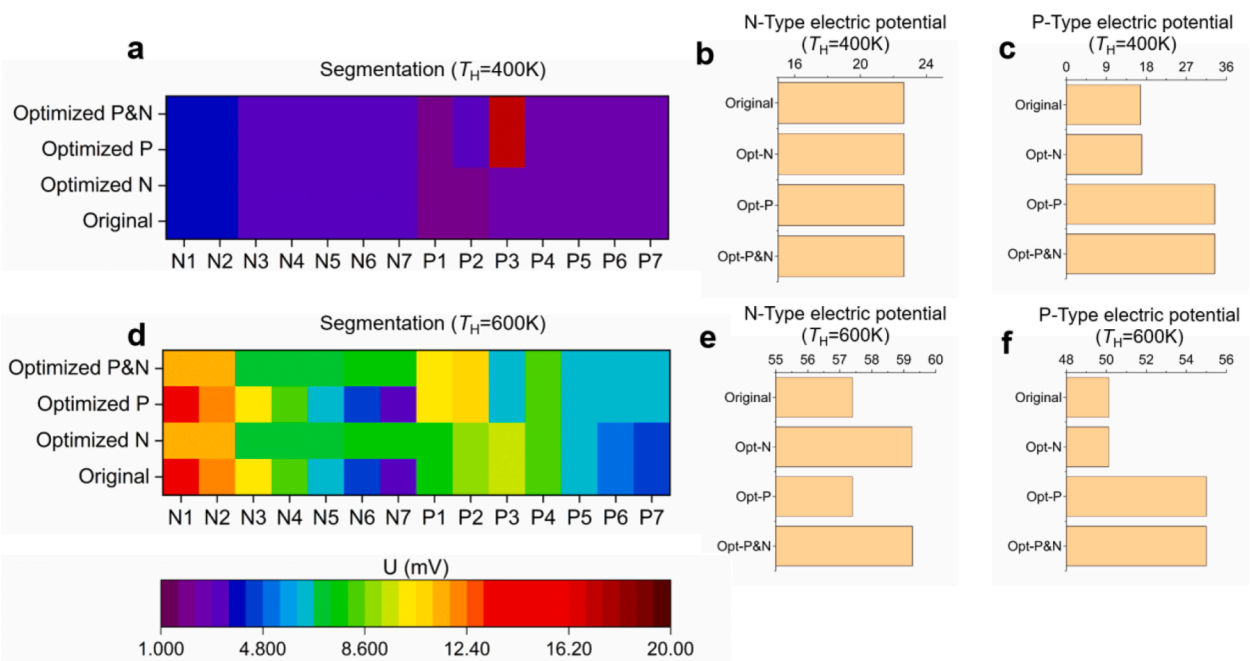

Fig. 9. Comparisons of the electric voltage value of each layer (a, d) and the entire leg (b, c, e, f) under the maximum power.

the P-type *ZT* of opt-P&N is 1.1831 which has a 9.03% increase compared with the origin. When $T_H = 600$ K, the N-type *ZT* value of opt-P&N is 0.8875 which is 67.78% higher than origin, and the P-type *ZT* value of opt-P&N is 1.1801 which is 4.57% lower than origin.

3.3. Performance under the maximum energy conversion efficiency

As shown in Table 4, under the condition of the maximum energy conversion efficiency, the best sequence of the P-type and N-type semiconductor legs are *ACDAAAA* and ACCCCCC when $T_H = 400$ K, the best sequence of the P-type and N-type semiconductor legs are *BBDADDD* and *ACDDDDD* when $T_H = 600$ K. As is shown in Fig. 11, opt-P&N is the highest and is dramatically higher than B and C. When $T_H = 400$ K, the power of opt-P&N is 27.6mW which is 81.57% higher than C which is highest among A, B, C and D, and is 0.4% lower than the corresponding performance under the maximum power. The open circuit voltage of opt-P&N is 56.5 mV which is 20.72% higher than C, and is 0.88% lower than the performance. The energy efficiency of opt-P&N is 13.71% which is 90.15% higher than A, and is 4.49% higher than the performance i. When $T_H = 600$ K, the power of opt-P&N is 131.9 mW which is 33.37% higher than D which is highest among A, B, C and D. The open circuit voltage of opt-P&N is 114.9 mV which is 2.96% higher

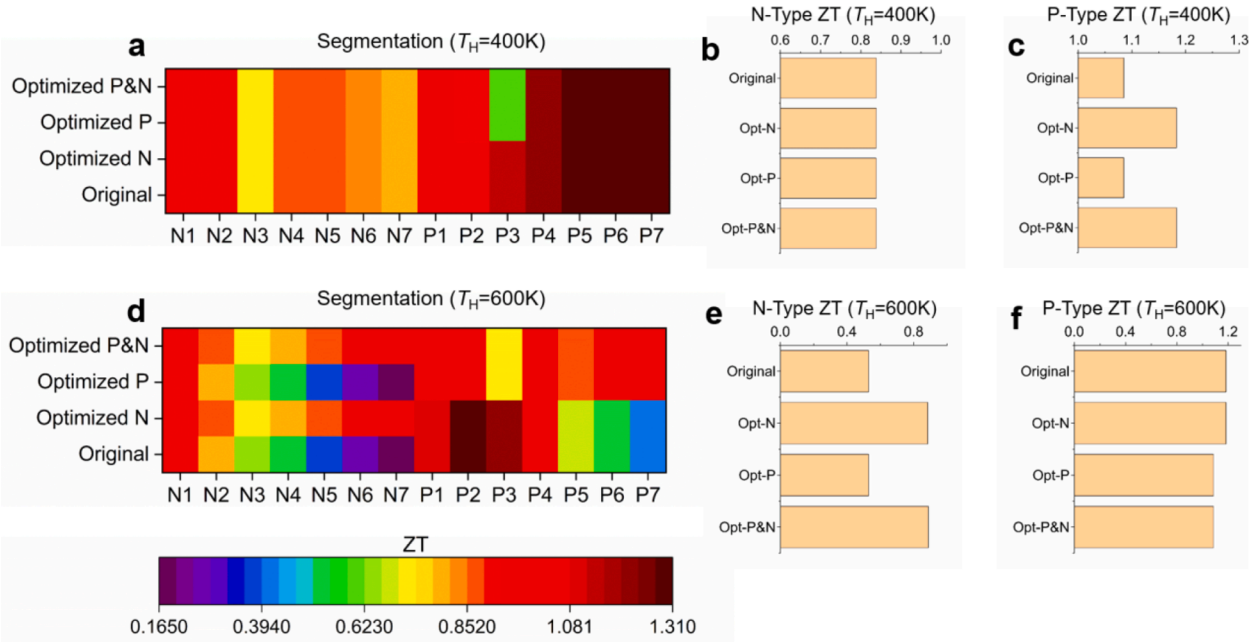

Fig. 10. Comparisons of the *ZT* value of each layer (a, d) and the entire leg (b, c, e, f) under the maximum power.

Table 4
optimal material sequences under the condition of maximum energy conversion efficiency.

	$T_H = 400$ K	$T_H = 600$ K
P-type	*ACDAAAA*	*BBDADDD*
N-type	*ACCCCCC*	*ACDDDDD*

than C, as shown in Fig. 9e. The energy efficiency of opt-P&N is 16.78% which is 31.19% higher than D. The power and energy efficiency is 28.35% lower and 8.33% higher than the power and energy efficiency under the maximum power, and the open circuit voltage of these two cases is nearly equal.

Fig. 12 illustrates the inner temperature distribution of the TEG when $T_H = 600$ K under the maximum energy conversion efficiency. For N-type semiconductor leg, the low temperature zone has wider distribution after optimization. But for the P-type semiconductor leg, things turn the opposite way. The temperature distribution of one semiconductor leg is almost unchanged after another one is optimized.

The comparisons of the electric resistance of each layer is shown in Fig. 13. When $T_H = 400$ K, the N-type electric resistance of opt-P&N is 16.83 mΩ which is 14.58% lower than origin, and the P-type electric resistance of opt-P&N is 9.81 mΩ which is 20.64% higher than origin. When $T_H = 600$ K, the N-type electric resistance of opt-P&N is 14.32 mΩ which is 62.97% lower than origin. And the P-type electric resistance of opt-P&N is 14.70 mΩ which is 4.18% higher than origin. With the raise of T_H, the total electric resistance is raising and the optimization tend to reduce the electric resistance. Compared with the electric resistance

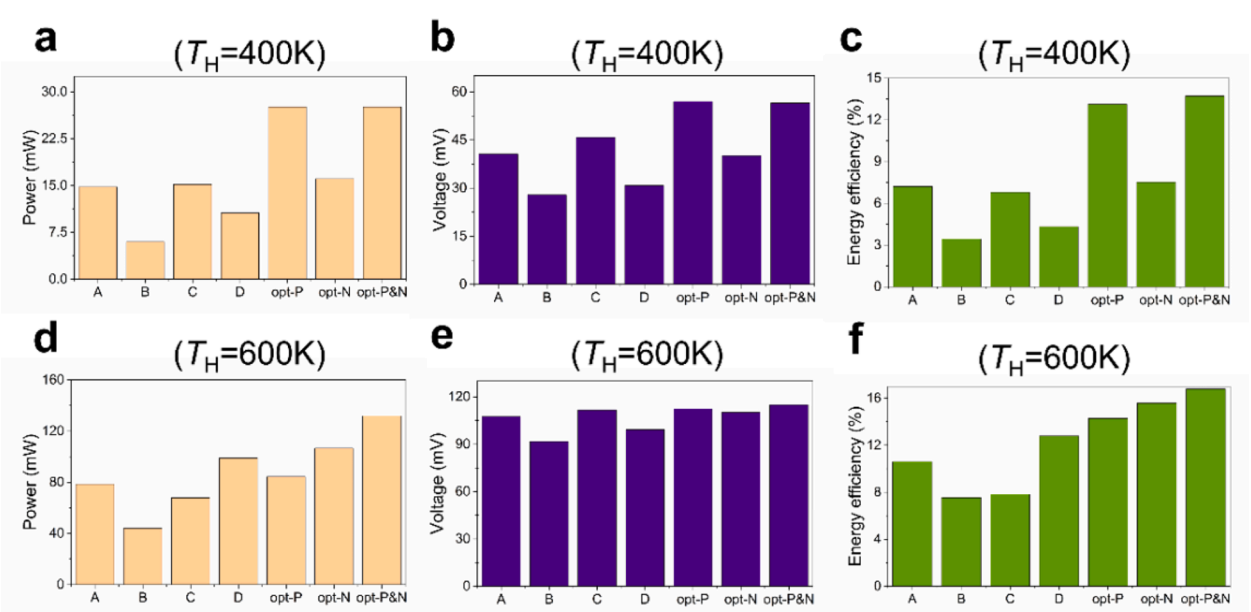

Fig. 11. Power (a, d) open circuit voltage(b, e), and energy efficiency(c, f) of different scenarios at two fixed temperature(400 K and 600 K) under the maximum energy conversion efficiency.

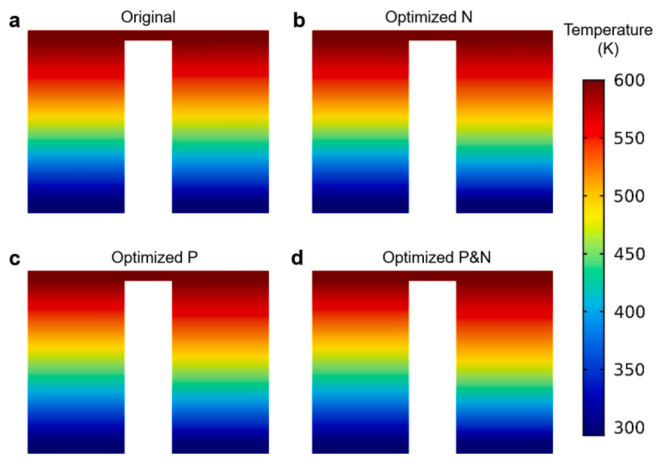

Fig. 12. Distribution of temperature of different scenarios when $T_H = 600$ K under the maximum energy conversion efficiency.

under the maximum power, optimization with the goal of maximum energy conversion efficiency reduces electric resistance more significantly.

Fig. 14 shows the open circuit voltage of each layer and the entire leg. When $T_H = 400$ K, the N-type open circuit voltage of opt-P&N is 23.12 mV which is 2.20% lower than origin, and the P-type open circuit voltage of opt-P&N is 33.41 which is 99.82% higher than the origin. When $T_H = 600$ K, the N-type open circuit voltage of opt-P&N is 59.94 mV which is 4.42% higher than origin, and the P-type open circuit voltage of opt-P&N is 55 mV which is 9.71% higher than origin. Strong evidence of the increase of electric voltage was found after the sequence of the semiconductor legs being optimized.

Fig. 15 shows the variation in *ZT* value of each layer and the entire leg. The *ZT* value of a leg is still unchanged after another leg is optimized. When $T_H = 400$ K, the N-type *ZT* value of opt-P&N is 0.8377 while the origin is 0.8382, and the P-type *ZT* of opt-P&N is 1.0851 which has 8.27% decrease compared with the origin. When $T_H = 600$ K, the N-type *ZT* value of opt-P&N is 0.8837 which is 67.02% higher than origin, and the P-type *ZT* value of opt-P&N is 0.9195 which is 4.59% higher than origin. It is obvious that the optimization dramatically increases *ZT* value especially when T_H is at a high level. Counterintuitively, the optimal sequence does not arrange in strict conformity with *ZT* value which has never been reported in the previous studies. Under the maximum energy conversion efficiency, when $T_H = 600$ K the best sequence of the P-type is *BBDADDD* while the first and second layers which are near the cold side are employed by material B which is a kind of medium-temperature TE material. As shown in Figs. 13–15, the electric resistance and *ZT* value of P1 and P2 increased and then decreased. But the voltage of P1 and P2 increased, which enhanced the performance due to the fact that the increase of voltage is more remarkable than that of the increase of electric resistance. Therefore, for obtaining the optimal material sequence, the Seebeck coefficients, electrical resistance, and the thermal conductivity should be considered in another compromised manner other than *ZT*.

3.4. Comparison of the power and cost

Table 5 shows the power and cost/power in previous studies and this work under specific conditions. In Ref.[39], the leg length under the condition we select is 6.22 mm, which leads to the low power density and high cost. In Ref.[40], we chose the SATEG(segmented annular thermoelectric generator) as the object, and in Ref. [41] the leg length of the object we select is 1.2 cm, but ΔT between of the hot side and cold side is 400 K, so the power is relatively high and the cost is reduced. Finally, in this work, we choose the best sequence when $T_H = 400$ K under the condition of maximum electric power. All the costs are from Refs. [24,41,39] and [42], and take the volume of each case into consideration, the cost/power of each case is calculated.

4. Conclusions

In this study, a seven-layer STEG is presented with four pairs of TE materials imposed on semiconductor legs. Firstly, the performance of the STEG with every possible combination (16384 material sequences) of the leg materials for either leg is analyzed when the other leg is equipped with selected material. Machine learning is further employed

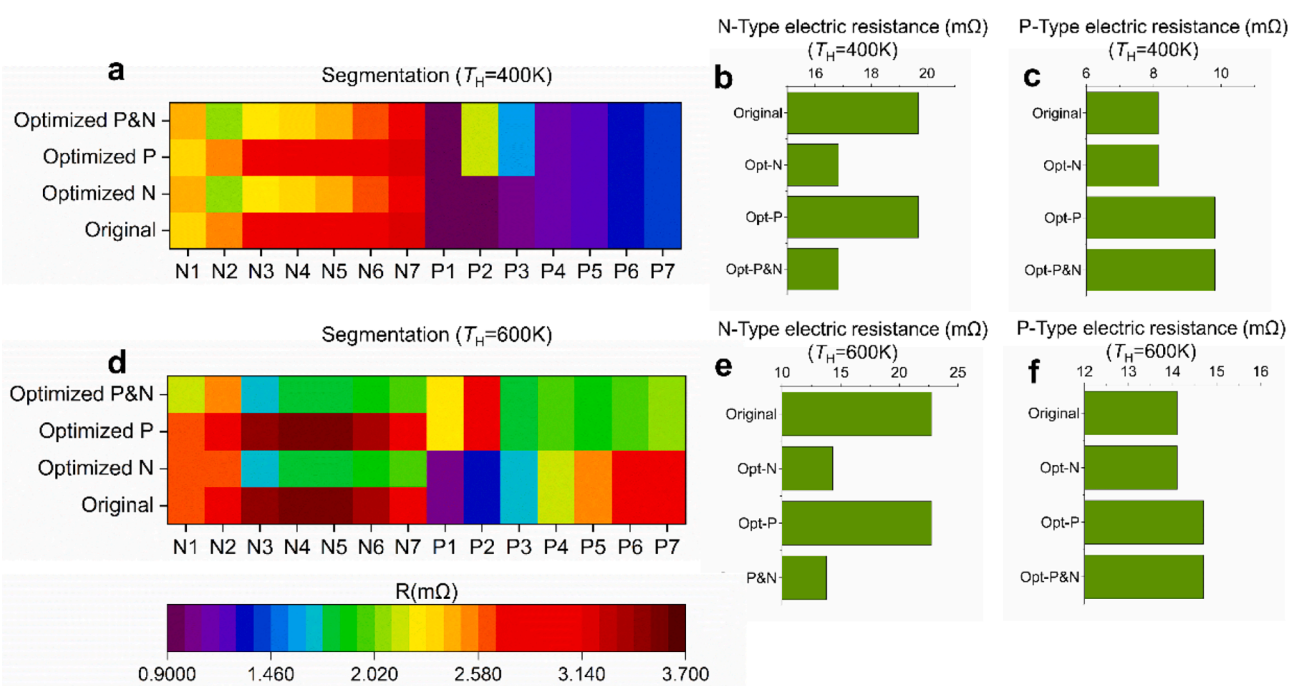

Fig. 13. Comparisons of the electric resistance of each layer (a, d) and the entire leg (b, c, e, f) under the maximum energy conversion efficiency.

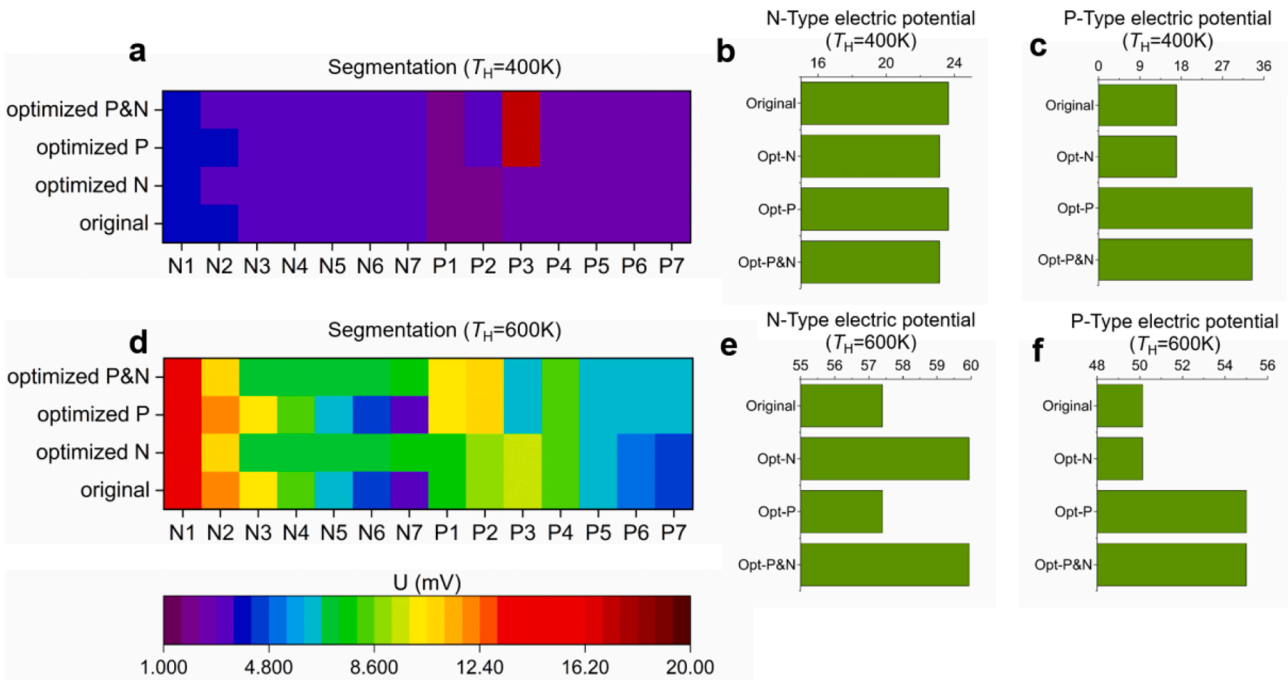

Fig. 14. Comparisons of the electric voltage of each layer (a, d) and the entire leg (b, c, e, f) under the maximum energy conversion efficiency.

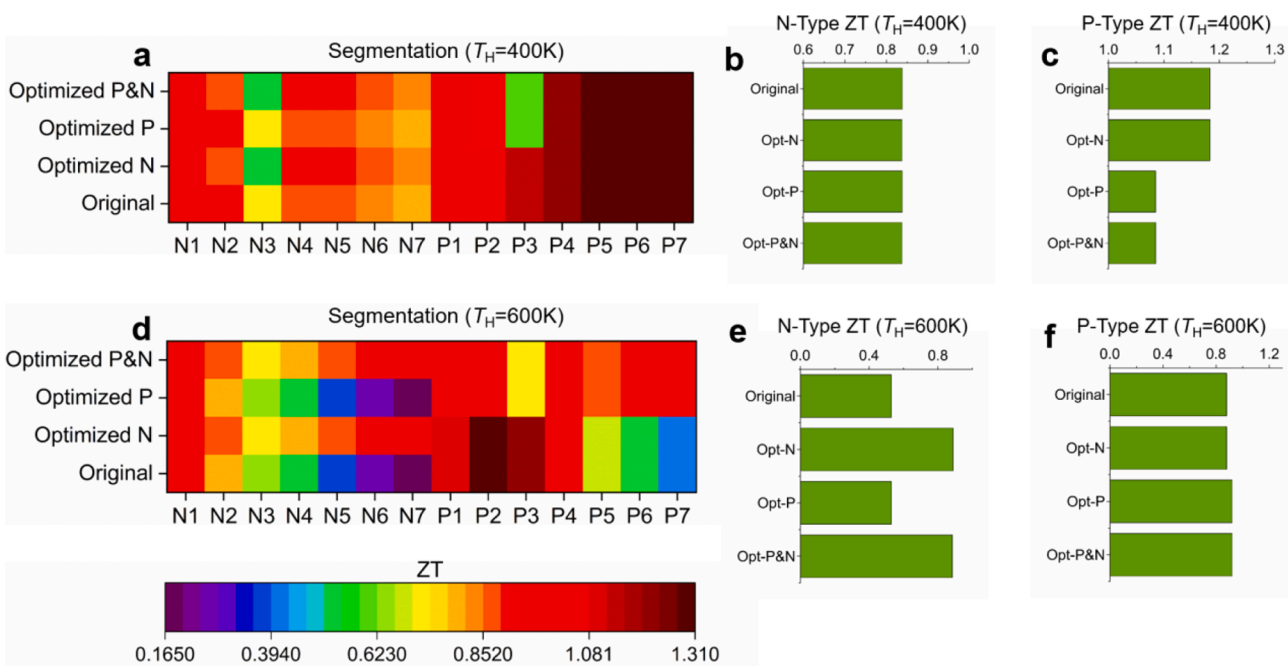

Fig. 15. Comparisons of the *ZT* value of each layer (a, d) and the entire leg (b, c, e, f) under the maximum energy conversion efficiency.

to reveal the relationship of the electric power and the energy conversion efficiency with the leg material sequences via the ensemble-based regression model whose hyper-parameters are adjusted by the Bayesian optimization. The criteria of maximum output power and maximum energy conversion efficiency are employed to identify the optimal material sequences for each semiconductor leg, and the overall optimal material sequences corresponding to the maximum power and energy conversion efficiency respectively. Compared with the traditional TEG, the segmented thermoelectric generators combined by different TE materials could enhance the output power and energy conversion efficiency significantly. When operating between 600 K and 293 K, the electric power and energy conversion efficiency of STEG is 184.1 mW and 16.7%, which presents enhancement of 86.14% and 31.19%, respectively. The temperature distribution, electric resistance, *ZT* value and open circuit voltage of each layer and the entire leg under the original, and partly optimized and overall optimized configures are systematically investigated. The optimal sequence does not arrange in strict conformity with *ZT* value. In certain temperature range, although the *ZT* value of a *TE* material is at a low level, the Seebeck coefficient is higher than the other material which leads to higher voltage, and the improvement of open circuit voltage override the impact of electric resistance, thus to augment the energy conversion efficiency. For

obtaining the optimal material sequence, the Seebeck coefficients, electrical resistance, and the thermal conductivity should be considered in another compromised manner other than *ZT*.

TE devices of 7 layers in each leg is investigated in present study, more layers increase contact electric resistance of STEG. With the contact electric resistance considered, the huge performance augmentation may not be realized. Further study should be conducted to resolve such issue and reveal the optimal layer numbers. Furthermore, experiments are also needed to validate the present findings.

CRediT authorship contribution statement

Junwei Zhao: Writing – original draft. **Wei Xu:** Visualization. **Zhengfei Kuang:** Visualization. **Rui Long:** Conceptualization, Writing - review & editing. **Zhichun Liu:** Investigation. **Wei Liu:** Formal analysis.

Declaration of Competing Interest

The authors declare that they have no known competing financial interests or personal relationships that could have appeared to influence the work reported in this paper.

Acknowledgements

This work was financially supported by the National Natural Science Foundation of China (52076088).

Appendix A

A1 Model validation

To validate the model employed in present study, we compared the calculated results with Hu et al.' experimental data [39]. As shown in Fig. A1, the data obtain via present model agrees well with Hu's experiment data. And the discrepancy between simulation and experiments is due to the ignorance of the contact electrical resistance in simulation.

A2. Temperature depended physical parameters of the TE materials

Thermal conductivity [$Wm^{-1}K^{-1}$]:

$$\lambda(T) = A_3 \times T^3 + A_2 \times T^2 + A_1 \times T^1 + A_0 \tag{A1}$$

Electrical conductivity [S/m]:

$$\sigma(T) = B_3 \times T^3 + B_2 \times T^2 + B_1 \times T^1 + B_0 \tag{A2}$$

Seebeck coefficient [V/K]:

Table 5
Comparison of power and cost/power.

	ΔT(K)	materials	Power(mW)	Cost/power($/W)
Ref. [39]	124.2	Bi_2Te_3	11.25	324.7
Ref. [40]	200	$(Bi,Sb)_2Te_3$, MgAgSb, $PbTe_{0.7}S_{0.3}$	100	2.3
Ref. [41]	400	Bi_2Te_3, $Yb_{0.2}InyCo_4Sb_{12}$, $Bi_{0.52}Sb_{1.48}Te_3$, $CeFe_4Sb_{12}$	325	1.5
This work	107	Listed in Table 2	27.7	1.2

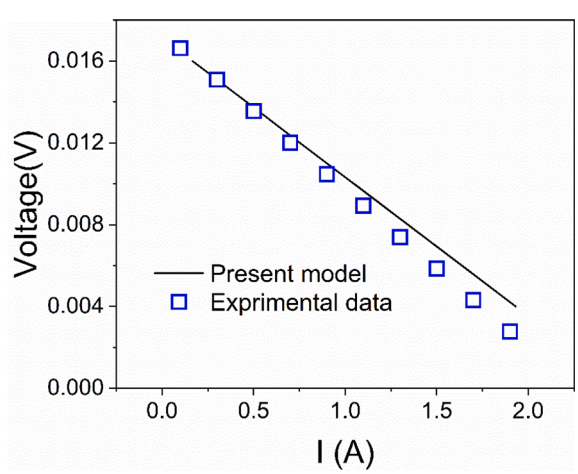

Fig. A1. Comparison of *I-V* curves between the data in present model and the data in Ref. [39].

Table A1
Parameters for calculating the thermal conductivity.

Material	A_3	A_2	A_1	A_0
N-A	0	1.19×10^{-5}	−0.00577	2.00418
P-A	0	3.11×10^{-5}	−0.02413	5.90208
N-B	0	1.65×10^{-5}	−0.01154	3.15454
P-B	0	1.50×10^{-5}	−0.01138	3.2729
N-C	-7.27×10^{-8}	1.21×10^{-4}	−0.0578	9.87
P-C	-9.53×10^{-8}	1.49×10^{-4}	−0.0686	11.41
N-D	2.4360×10^{-9}	-4.4576×10^{-6}	3.0553×10^{-3}	1.4464
P-D	1.2202×10^{-8}	-2.4031×10^{-5}	1.6390×10^{-2}	−2.066

Table A2
Parameters for calculating the electrical conductivity.

Material	B_3	B_2	B_1	B_0
N-A	0	0.89631	−860.754	262,854
P-A	0	1.80184	−2101.88	686731.8
N-B	0	1.08586	−1131.212	355392.55
P-B	0	1.23316	−1306.01	386050.87
N-C	-1.21×10^{-3}	2.56	−1643	398,905
P-C	-1.88×10^{-3}	3.56	−2196	490,233
N-D	-6.09981×10^{-5}	0.27153	−318.102	209899.2
P-D	4.41749×10^{-5}	0.07026	−201.233	183930.4

Table A3
Parameters for calculating the Seebeck coefficient.

Material	C_3	C_2	C_1	C_0
N-A	0	2.31×10^{-9}	-1.65×10^{-6}	6.89×10^{-5}
P-A	0	-1.30×10^{-9}	1.17×10^{-6}	8.8×10^{-5}
N-B	0	1.86×10^{-10}	-3.34×10^{-7}	-4.58×10^{-5}
P-B	0	-3.13×10^{-10}	4.82×10^{-7}	-5.1764×10^{-6}
N-C	-4.51×10^{-12}	7.61×10^{-9}	-3.74×10^{-6}	3.5005×10^{-4}
P-C	4.03×10^{-12}	-8.23×10^{-9}	4.41×10^{-6}	-4.8841×10^{-4}
N-D	1.4197×10^{-13}	2.4331×10^{-11}	-2.734×10^{-7}	-7.2398×10^{-5}
P-D	-5.0917×10^{-13}	5.5507×10^{-10}	-3.6827×10^{-10}	8.8139×10^{-5}

$$\alpha(T) = C_3 \times T^3 + C_2 \times T^2 + C_1 \times T^1 + C_0 \tag{A3}$$

References

[1] Araiz M, Casi Á, Catalán L, Martínez Á, Astrain D. Prospects of waste-heat recovery from a real industry using thermoelectric generators: Economic and power output analysis. Energy Convers Manage 2020;205:112376. https://doi.org/10.1016/j.enconman.2019.112376.

[2] Long R, Li B, Liu Z, Liu W. Performance analysis of a solar-powered electrochemical refrigerator. Chem Eng J 2016;284:325–32.

[3] Long R, Kuang Z, Liu Z, Liu W. Ionic thermal up-diffusion in nanofluidic salinity-gradient energy harvesting. Natl Sci Rev 2019;6(6):1266–73.

[4] Lai X, Long R, Liu Z, Liu W. A hybrid system using direct contact membrane distillation for water production to harvest waste heat from the proton exchange membrane fuel cell. Energy 2018;147:578–86.

[5] Long R, Li B, Liu Z, Liu W. Performance analysis of a dual loop thermally regenerative electrochemical cycle for waste heat recovery. Energy 2016;107:388–95.

[6] R. Long, X. Xia, Y. Zhao, S. Li, Z. Liu, W. Liu, Screening metal-organic frameworks for adsorption-driven osmotic heat engines via grand canonical Monte Carlo simulations and machine learning, iScience 24(1) (2021) 101914.

[7] Zhao Y, Li M, Long R, Liu Z, Liu W. Dynamic modelling and analysis of an adsorption-based power and cooling cogeneration system. Energ Convers Manage 2020;222:113229.

[8] Leonov V. Thermoelectric Energy Harvesting of Human Body Heat for Wearable Sensors. IEEE Sens J 2013;13(6):2284–91.

[9] Proto A, Peter L, Cerny M, Penhaker M, Bibbo D, Conforto S, et al. Human Body Energy Harvesting Solutions for Wearable Technologies. In: 2018 IEEE 20th International Conference on e-Health Networking, Applications and Services (Healthcom); 2018. p. 1–5.

[10] Guan M, Wang K, Xu D, Liao W-H. Design and experimental investigation of a low-voltage thermoelectric energy harvesting system for wireless sensor nodes. Energy Convers Manage 2017;138:30–7.

[11] Glatz W, Schwyter E, Durrer L, Hierold C. $\hbox{Bi}_{2}\hbox{Te}_{3}$-Based Flexible Micro Thermoelectric Generator With Optimized Design. J Microelectromech Syst 2009;18(3):763–72.

[12] Liu C, Pan X, Zheng X, Yan Y, Li W. An experimental study of a novel prototype for two-stage thermoelectric generator from vehicle exhaust. J Energy Inst 2016;89(2):271–81.

[13] Liu K, Tang X, Liu Y, Yuan Z, Li J, Xu Z, et al. High-performance and integrated design of thermoelectric generator based on concentric filament architecture. J Power Sources 2018;393:161–8.

[14] Yuan Z, Tang X, Xu Z, Li J, Chen W, Liu K, et al. Screen-printed radial structure micro radioisotope thermoelectric generator. Appl Energy 2018;225:746–54.

[15] Zhou Y, Li L, Tan Q, Li J-F. Thermoelectric properties of Pb-doped bismuth telluride thin films deposited by magnetron sputtering. J Alloy Compd 2014;590:362–7.

[16] Sreeram PR, Ganesan V, Thomas S, Anantharaman MR. Enhanced thermoelectric performance of nanostructured manganese telluride via antimony doping. J Alloy Compd 2020;836:155374.

[17] Jiang J, Chen L, Bai S, Yao Q, Wang Q. Thermoelectric properties of textured p-type (Bi, Sb)2Te3 fabricated by spark plasma sintering. Scr Mater 2005;52(5):347–51.

[18] He Z, Chen Y-X, Zheng Z, Li Fu, Liang G, Luo J, et al. Enhancement of thermoelectric performance of N-type Bi2Te3 based thin films via in situ annealing during magnetron sputtering. Ceram Int 2020;46(9):13365–71.

[19] Choi H, Jeong K, Chae J, Park H, Baeck J, Kim TH, et al. Enhancement in thermoelectric properties of Te-embedded Bi2Te3 by preferential phonon scattering in heterostructure interface. Nano Energy 2018;47:374–84.

[20] Guo D, Li C, Li K, Shao B, Chen D, Ma Y, et al. The strain-induced excellent thermoelectric performance of PbTe. Physica E 2021;130:114685. https://doi.org/10.1016/j.physe.2021.114685.
[21] Yang Z, Wang S, Sun Y, Xiao Y, Zhao L-D. Enhancing thermoelectric performance of n-type PbTe through separately optimizing phonon and charge transport properties. J Alloy Compd 2020;828:154377.
[22] Lue CS, Chen SC. Evolution of the electronic structure in partially filled skutterudites: CaxCo4Sb12 studied using NMR. Physical Review B 2009;79(12).
[23] Ye LY, Wang YX, Yang JM, Yan YL, Zhang JH, Guo LB, et al. Electronic structure and thermoelectric properties of the Zintl compounds Sr5Al2Sb6 and Ca5Al2Sb6: first-principles study. RSC Adv. 2015;5(63):50720–8.
[24] Zhang G, Fan L, Niu Z, Jiao K, Diao H, Du Q, et al. A comprehensive design method for segmented thermoelectric generator. Energy Convers Manage 2015;106:510–9.
[25] Shittu S, Li G, Zhao X, Ma X, Akhlaghi YG, Ayodele E. High performance and thermal stress analysis of a segmented annular thermoelectric generator. Energy Convers Manage 2019;184:180–93.
[26] El-Genk MS, Saber HH. High efficiency segmented thermoelectric unicouple for operation between 973 and 300 K. Energy Convers Manage 2003;44(7):1069–88.
[27] El-Genk MS, Saber HH, Caillat T. Efficient segmented thermoelectric unicouples for space power applications. Energy Convers Manage 2003;44(11):1755–72.
[28] Zhu L, Li H, Chen S, Tian X, Kang X, Jiang X, et al. Optimization analysis of a segmented thermoelectric generator based on genetic algorithm. Renewable Energy 2020;156:710–8.
[29] Li S, Pei J, Liu D, Bao L, Li J-F, Wu H, et al. Fabrication and characterization of thermoelectric power generators with segmented legs synthesized by one-step spark plasma sintering. Energy 2016;113:35–43.
[30] Shen Z-G, Liu X, Chen S, Wu S-Y, Xiao L, Chen Z-X. Theoretical analysis on a segmented annular thermoelectric generator. Energy 2018;157:297–313.
[31] Liu H-B, Meng J-H, Wang X-D, Chen W-H. A new design of solar thermoelectric generator with combination of segmented materials and asymmetrical legs. Energy Convers Manage 2018;175:11–20.
[32] Lundgaard C, Sigmund O. Design of segmented thermoelectric Peltier coolers by topology optimization. Appl Energy 2019;239:1003–13.
[33] Sun H, Ge Ya, Liu W, Liu Z. Geometric optimization of two-stage thermoelectric generator using genetic algorithms and thermodynamic analysis. Energy 2019;171:37–48.
[34] Ge Ya, Liu Z, Sun H, Liu W. Optimal design of a segmented thermoelectric generator based on three-dimensional numerical simulation and multi-objective genetic algorithm. Energy 2018;147:1060–9.
[35] He H, Wu Yi, Liu W, Rong M, Fang Z, Tang X. Comprehensive modeling for geometric optimization of a thermoelectric generator module. Energy Convers Manage 2019;183:645–59.
[36] Chen W-H, Chiou Y-B. Geometry design for maximizing output power of segmented skutterudite thermoelectric generator by evolutionary computation. Appl Energy 2020;274:115296.
[37] Fraisse G, Ramousse J, Sgorlon D, Goupil C. Comparison of different modeling approaches for thermoelectric elements. Energy Convers Manage 2013;65:351–6.
[38] Wang X-D, Huang Y-X, Cheng C-H, Ta-Wei Lin D, Kang C-H. A three-dimensional numerical modeling of thermoelectric device with consideration of coupling of temperature field and electric potential field. Energy 2012;47(1):488–97.
[39] Hu X, Yamamoto A, Ohta M, Nishiate H. Measurement and simulation of thermoelectric efficiency for single leg. Rev Sci Instrum 2015;86(4):045103. https://doi.org/10.1063/1.4916545.
[40] Ouyang Z, Li D. Design of segmented high-performance thermoelectric generators with cost in consideration. Appl Energy 2018;221:112–21.
[41] Tian M-W, Mihardjo LWW, Moria H, Asaadi S, Sadighi Dizaji H, Khalilarya S, et al. A comprehensive energy efficiency study of segmented annular thermoelectric generator; thermal, exergetic and economic analysis. Appl Therm Eng 2020;181:115996.
[42] LeBlanc S, Yee SK, Scullin ML, Dames C, Goodson KE. Material and manufacturing cost considerations for thermoelectrics. Renew Sustain Energy Rev 2014;32:313–27.